Materials Science & Engineering A 943 (2025) 148774

Contents lists available at ScienceDirect

Materials Science & Engineering A

journal homepage: www.elsevier.com/locate/msea

Inverse Hall-Petch and nanocrystal-amorphous transition of broad-spectrum W content NiW alloys

Zhifei Yu [a], Shaojia Shi [a], Xingwen Zhang [a], Zesheng You [c], Yonghao Zhao [a,b,*]

[a] Nano and Heterogeneous Materials Center, School of Materials Science and Engineering, Nanjing University of Science and Technology, Nanjing, 210094, China
[b] School of Materials Science and Engineering, Hohai University, Changzhou, 213200, China
[c] Herbert Gleiter Institute of Nanoscience, School of Materials Science and Engineering, Nanjing University of Science and Technology, Nanjing, 210094, China

ARTICLE INFO

Keywords:
Electrodeposition
Nickel-tungsten
Inverse Hall-Petch
Nanocrystal-amorphous

ABSTRACT

Fabricating metallic materials with grain sizes below 10 nm, particularly in the range between 2.4 and 7.2 nm, poses a challenge. However, it is crucial to accurately identify Hall-Petch breakdown within this range. Moreover, there are differing opinions regarding the change in strength that occurs when nanocrystals transform into amorphous materials. This study involved the electroplating preparation of amorphous or nanometer NiW coatings spanning 1.9–15.8 nm by adjusting current density and temperature. The microstructure under tungsten atoms solid solution was characterized and measured surface hardness. The results revealed that the tungsten solid solution in FCC Ni alloy refines grain size and the strength follows the Hall-Patch relationship while the hardness of nanocrystal NiW alloy with 12.3 at% W regional maximum at 7.79 GPa at the critical point of 5.9 nm, significantly surpassing the 5.29 GPa hardness of pure nickel at 22.0 nm. After that, reverse Hall-Petch abnormal phenomenon begin. The annealed alloy of Ni-15.0 at% W had the similar trend and critical point at 5.0 nm. Following the transformation into an amorphous state, hardness further rises, reaching a pinnacle of 8.95 GPa of Ni-20.9 at%W. The values of solid solution hardening under various content of tungsten atoms were calculated. It suggests that the solid solution limitation of nanocrystal NiW which grain size bellowed 10.0 nm expanded. After removing the hardening by atoms solid solution, the similar Hall-Petch breakdown phenomenon was observed while the critical point was expansion offset to 8.6 nm which was approaching the critical point of nickel electrodeposited coating.

1. Introduction

Nanomaterials have been a primary focus of research across various fields due to their unique nanoscale effects. The strength of metal materials demonstrates a linear increase as grain size decreases [1,2]. Hall-Petch relation quantifies the direct growth correlation between crystal strength and the reciprocal square root of grain size. Nonetheless, this strengthening relationship breaks down at extremely small grain sizes, typically around 5–30 nm, leading to a Hall-Petch failure mechanism [3–5]. In this context, there exists a strengthening limit, namely the critical grain size associated with the inverse Hall-Petch relationship. Simultaneously, the critical point is influenced by the overall grain size of the material, shifting towards smaller grain sizes and consequently extending the Hall-Petch relationship and obtaining the maximum strength [6]. As the grain size of the nanocrystals diminishes, there is a tendency for the crystals to transition towards an amorphous state. This conversion not only holds scientific intrigue but also establishes the physical boundary for strengthening nanostructured engineering materials [3]. Furthermore, numerous intriguing questions persist regarding material behavior at the finest nanocrystalline and amorphous. Hence, it is essential to fabricate corresponding materials and investigate the critical point of the Hall-Petch relation specifically the pivotal transition trend from multiple nanocrystals to amorphous state.

Nanocrystalline Ni fabricated via electrodeposition has been extensively investigated [4,7,8]. Its grain size can be further reduced through the solid solution of Mo, W, Nb, and other refractory metal due to suppress grain boundary diffusion by decreasing grain boundary diffusivity [9]. In general, the tungsten content in NiW alloy by electrodeposition affects the formation of crystalline and microstructure. Diverse structures demonstrate variations in mechanical performance when

---

[*] Corresponding author. Nano and Heterogeneous Materials Center, School of Materials Science and Engineering, Nanjing University of Science and Technology, Nanjing, 210094, China.

E-mail address: yhzhao@njust.edu.cn (Y. Zhao).

https://doi.org/10.1016/j.msea.2025.148774
Received 27 April 2025; Received in revised form 20 June 2025; Accepted 4 July 2025

applied. However, the investigation of the tungsten content range in NiW through electrodeposition technology remains limited, with inconsistencies in the exploration of its mechanical properties [9]. Furthermore, wide distribution grain size of NiW alloys, particularly within the precise range from 2.4 nm to 7.2 nm range, have rarely been fabricated. This hindered the accurate exploration of the specific value of the characteristic point of the Hall-Petch breakdown relationship [6]. Therefore, it holds significant importance and value to adjust the processing methods to obtain niobium-containing tungsten and conduct relevant research.

Similar to Nc alloys materials, amorphous alloys have been not only extensively studied in fundamental research, but also of interest in potential applications. The advantages of the amorphous alloy such as high hardness, high corrosion and excellent wear resistance make them as a good candidate for many applications [10,11]. Electrodeposition of NiW coatings has demonstrated the ability to produce amorphous materials, including nanocrystalline/amorphous biphasic materials [12–15]. For the NiW electrodeposition coatings, the crystalline structure is changed to amorphous state when the tungsten content reaches the critical value of 20 at% [16,17]. The relate high quality amorphous and nanocrystalline NiW based alloys with premium and unique high temperature and mechanical properties. However, the underlying mechanism involving the interactions and transformation between nanocrystalline and amorphous phases is still under exploring.

In a brief, surface electrodeposited NiW coatings serve as excellent materials for studying Hall-Petch breakdown even the transfer from nanometer to amorphous phases. Under the condition of easily deposited with particle sizes ranging from nanometer to amorphous phases, exhibiting high quality, low stress, and non-porous deposits [18]. Based on this foundation, theoretical support is conducted on the mechanical properties, friction, oxidation, and corrosion of NiW electroplated coatings. Chun et al. [6], explored the Hall-Petch relationship via high tungsten content NiW (15.5–23.0 at%W) electrodeposited alloys and predicted the critical Hall-Petch grain size around 5 nm. Giga et al. [19], discussed the inverse Hall-Petch relationship via tensile testing from NiW electrodeposited alloys with different tungsten content and grain size which indicated that the critical grain size was around 8 nm. Wu et al. [20], prepared NiW (39 wt%-50 wt%) alloys and suggested that the high tungsten content delayed the Hall-Petch breakdown critical point to 4.5 nm. Schuh et al. [3], found that the solid-solution strengthening contribution to be 40 MPa (5 %), which is almost negligible compared to the intrinsic hardness of nickel (800 MPa) under grain size strengthening. While, it was found that this may begin somewhere above W-rich NiW (13 at%) [6]. Previous studies investigating the breakdown point of the Hall-Petch relationship have predominantly employed NiW electroplated alloys with high tungsten content to regulate grain size. This approach, however, introduces additional variables that may limit the generalizability of the results. Hence, it is scientifically meaningful to adopt a broad-spectrum tungsten content NiW alloy with varieties grain size and excluded the subtle influence of solid solution, i.e. nickel.

In this work, eight sets of nanocrystalline NiW alloys with varying tungsten content (0.5–15.0 at%) and grain sizes (15.8–1.9 nm) alongside pure nickel were fabricated by adjusting the current density and temperature during the electroplating process. Additionally, two groups of amorphous NiW alloy samples were prepared. The investigation focused on studying the relationship between tungsten content, grain size, microstructure, and strength. By employing fitting and calculations, we determined the limit of the synergistic strengthening effect of grain boundary and solid-solution. Furthermore, the critical point of the anomalous phenomenon in the Hall-Petch relation were identified, shedding light on the previously unaddressed phenomenon of hardness exhibiting a continuous increase post the nanocrystalline to amorphous transformation.

2. Experiments

2.1. Materials and preparation

Sodium hydroxide (NaOH), Sodium carbonate (Na_2CO_3), Sodium phosphate (Na_3PO_4) and lauryl sodium sulfate (SDS) for substrate predegreased, hydrochloric acid (HCl) for excitation and nickel sulfate hexahydrate ($NiSO_4 \cdot 6H_2O$), sodium tungstate dihydrate ($Na_2WO_4 \cdot 2H_2O$), sodium citrate dihydrate ($Na_3C_6H_5O_7 \cdot 2H_2O$), ammonium chloride ($NH_4CL$), sodium bromide (NaBr) as electrodeposition medium were purchased from Sinopharm Chemical Reagent Co., Ltd. All reagents were used without further purification.

30CrNi2MoV steel served as the substrate material for the electrodeposition. The anode was pure nickel plate. To achieve a flat and smooth surface, the surface of the 30CrNi2MoV steel to be plated undergoes a sequential polishing process using 80#, 600#, 1500#, and 2000# sandpaper. Following this, a diamond abrasive pastes with grain sizes of 1.0 μm is applied and polished until a mirror-like finish is obtained. Finally, the surface is thoroughly ultrasonic rinsed with deionized water and ethyl alcohol for 10 min respectively. Pre-treatment process as an electrodeposition substrate is as following: the stain coupon was immersed in degreased fluid at 50 °C for 3 min. After rinsing with deionized water, immerse the coupon in a 2 wt% HCl for 0.5 min for activation.

The electrodeposition was carried out in a plating bath utilizing specific aqueous bath chemistry. The composition of the electrodeposited media, including its components and their respective concentrations, has been optimized and refined based on prior research [21], as illustrated in Table 1. In this process, the 30CrNi2MoV is submerged in 0.25L electroplating solution as the cathode, while the anode plate is positioned opposite to the surface of the cathode, with a spacing of 4 cm. The current for electrodeposition process was regulated by adjustable double pulse power supply (SOYI-3010DM) supply purchased from Shanghai Soyi Electronic Technology Co., LTD. Note that a new electroplating solution replaced for each preparation of the NiW alloy coatings.

2.2. Microstructural characterizations

Elemental compositions specifically tungsten content was appraised on a field emission scanning electron microscope (SEM, Quanta 250F) equipped with an energy dispersive spectrometer (EDS). At least three plots are characterized to determine errors of tungsten atomic content. X-ray diffractometer (XRD) by a Bruker D8 was carried out with Cu–Kα radiation between 30° and 90° to analyze the phase structures of coatings. Grain size and lattice parameter were calculated from Ni (111) peak of full width at half maximum (FWHM) at around $2\theta = 44.1^\circ$ of NiW alloys XRD spectra, after correcting for instrumental broadening under support of Scherrer formula [22]. Calculate three times for each sample to determine the error. The microstructures were characterized on Aberration correction transmission electron microscopy at sub-Angstrom resolution (Titan G2 60–300) and samples for high resolution transmission electron microscopy (HR-TEM) observation were prepared by focused ion beam (FIB) system in order to statistical grain size. The microstructure of samples was investigated qualitatively by ex-situ cross-sectional FIB observation. In order to obtain a quantitative measure of the grain growth in-situ XRD measurements were also

Table 1
Composition of medium and deposition parameters.

$NiSO_4 \cdot 6H_2O$	0.060 M	pH	8–9
$Na_2WO_4 \cdot 2H_2O$	0.080 M	Temperature (K)	333–363
$Na_3C_6H_5O_7 \cdot 2H_2O$	0.400 M	Time (h)	1
NH_4CL	0.500 M	Current density $A \cdot dm^{-2}$	10–40
NaBr	0.150 M	Rotation rate (rpm)	~1200

performed during heat treatment.

2.3. Annealing treatment

NiW with 15.0 at% W electrodeposited coating was annealed in a tube furnace under a protective atmosphere of Ar atmosphere. The growth of grains and softening of materials shall be tested after being kept at 673K, 873K, 973K and 1073K for 2 h for subsequent testing. In order to ensure that the changes in microstructure were solely caused by the heat treatment, one sample from each condition was cut into blocks using an electrical discharge wire cutting machine, and each block was annealed at different temperatures or aging time respectively.

2.4. Hardness

Vickers microhardness of NiW alloys and annealed coupons was measured by HMV-G 21DT digital tester with a 980.7 mN load (HV0.1) and a 15-s dwell time. In order to avoid the interference from the substrate on microhardness measurements, a low load was selected to ensure that the depth of the indentation was significantly smaller than the NiW coatings thickness (approximately 30–50 μm). Each coupon underwent a minimum of 8 well-distributed measurements, followed by the determination of the average value and error bars.

3. Results

3.1. Process and composition of NiW coatings

The elemental composition, particularly the tungsten content and microstructure, is critical in influencing mechanical performance. Furthermore, it is well-established that process parameters significantly affect the properties of electrodeposited coatings. After determining the composition of the plating solution, temperature and current density emerge as the most crucial process parameters. Typically, high current density can result in enhanced tungsten content and microhardness in the electrodeposited coatings [23]. In present work, NiW electrodeposited alloys with a broad range of tungsten content from 0.5 at% to 20.9 at% was generated by controlling current density and temperature during electrodeposition which is shown in Fig. 1 (a). Among them, NiW alloy coating with the highest tungsten content (20.9 at% W), was obtained from a high current density of 35 A dm^{-2} at 348K. Besides, the relationship curves between tungsten content and electrodeposition parameter are shown in Fig. 1 (b). At the same temperature, the tungsten content of NiW electrodeposited coatings continuously increases with the rising current density. At lower temperatures (333K), the variation in tungsten content relative to current density is relatively gradual and remains consistently within a moderate range. At the appropriate temperature (348K), the tungsten content rises significantly in response to changes in current density. This is because that increasing the temperature within a specific range (around 333K) will accelerate the ion diffusion rate and lower the co-deposition potential threshold, thereby enhancing electrodeposition. While in ammonia-containing systems, an increase in temperature (especially at 363K) may lead to decomposition and a reduction in pH. At this juncture, current density becomes the primary factor influencing deposition, and tungsten content exhibits a linear relationship with current density.

XRD characterization is the most suitable method for studying nanocrystals with exceptionally small grain size (< 10 nm) which can analyze and determine crystal properties, phase composition, grain size, and lattice constants. XRD patterns of NiW alloys with broad rage tungsten atomic contents are shown in Fig. 2 (a). All the electrodeposited NiW nanocrystals alloys exhibit peaks at around 44.4° represent the γ-Ni, this inference is consistent with JCPDS No. 65–2865 [24]. With the increase in tungsten content, the (111) diffraction peak of Ni exhibits a gradual broadening trend, indicating a corresponding decrease in grain size. When the tungsten content exceeds 15.0 at%, an amorphous diffraction peak appears, revealing that the increase in tungsten content leads to the transformation from nanocrystals to an amorphous state. Furthermore, the intensity of the amorphous diffraction peak of the NiW coating containing 20.9 at% W diminishes to a level that becomes difficult to detect. Additionally, the diffraction peak of the nickel (111) crystal plane occasionally shifts to a lower angle as a result of the tungsten atom solution [24]. Furthermore, no additional phase was identified in the XRD patterns, despite surpassing the solid solubility limit of tungsten atoms in nickel about 10.0 at% [15,25–27]. This observation may be attributed to the electrodeposition of metastable or non-equilibrium solid solutions, or to an associated increase in the solid solution limit at ultrafine grain sizes [14]. The NiW alloy containing 15.0 at% W (348K-30 A dm^{-2}) was subjected to annealed for 2 h at temperatures of 673K, 873K, 973K and 1073K, respectively, the corresponding XRD characterization results are presented in Fig. 2 (b). Under the influence of high temperature, the (111) diffraction peak of nickel gradually narrows with rising temperature, indicating an increase in grain size. Additionally, the XRD spectrum of the annealed coupons did not exhibit any diffraction peaks corresponding to other phases, indicating that the alloy had not undergone a phase transition.

The effects and relationship curves of current density and temperature parameters of the electrodeposited process on the grain size of the NiW coatings are shown in Fig. 2(c) and (d). At lower temperatures or current densities, NiW exhibit larger grain sizes surpassing 10.0 nm. As these parameters increase, the intensified deposition and solid solution of tungsten consume some of the energy required for grain nucleation and growth, resulting in smaller grain sizes below 10 nm, within a minimum of 1.9 nm. Notably, Ni-12.3 at%W prepared under high-temperature and overvoltage conditions (363K-30 A dm^{-2}) exhibits an unusual phenomenon, characterized by relatively larger grain size (5.9

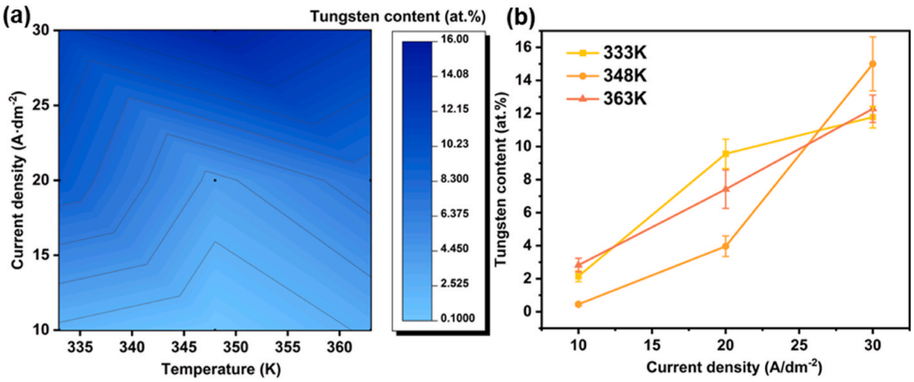

Fig. 1. Preparation and composition of NiW alloys. Relationship mapping (a) and curves (b) between electrodeposition parameter and tungsten content of NiW electrodeposited alloys.

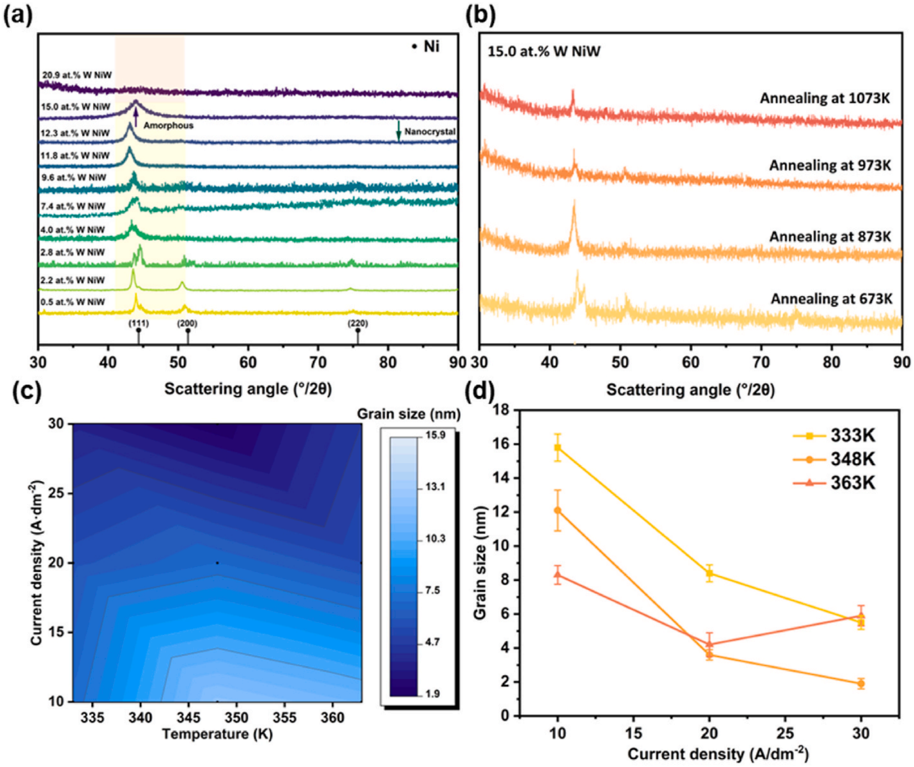

Fig. 2. XRD and grain size of NiW alloys. XRD patterns of NiW alloys with different tungsten atomic content (a), NiW (15.0 at% W) alloys annealed at different temperature for 2 h (b) and relationship mapping (c) and curves (d) between grain size and electrodeposited parameter.

nm). This observation is attributed to the excess energy supplied by the system, which facilitates crystal growth. Consequently, this accelerates the growth rate beyond the nucleation rate [21].

3.2. Microstructure and grain size

The microstructure images of nanocrystal NiW coatings with 2.8 at% W (363K-10 A dm^{-2}) and 7.4 at% (363K-20 A dm^{-2}) W were charactered by HR-TEM shown in Fig. 3 (a) and (b) respectively. Electron diffraction patterns were corresponding displayed to determine the property of alloys crystal. For the microstructure, the nanocrystal of NiW alloys with 2.8 at% W and 7.4 at% W, both of them are densely populated with a substantial number of equiaxed nanocrystals and exhibit homogeneous rings from polycrystalline suggestive of a well-randomized texture. The distribution of NiW alloys nanocrystal grain size statistics is depicted in Fig. 3 (c). One hundred grains were counted in each sample within the field of view, with average grain sizes of 9.0 nm for Ni-2.8 at% W and 5.6 nm for Ni-7.4 at% W. These statistical findings align closely with those determined through XRD calculations of grain size in nickel (111). In addition, it is expected that more tungsten atoms in solid solution will lead to a decrease in grain size.

For the NiW with 12.3 at% W (363K-30 A dm^{-2}), the TEM image was shown in Fig. 4 (a). Similar to nanocrystals, this sample exhibits a random grains orientation and densely arranged equiaxed grains. Although the tungsten content in the alloy surpasses the solid solution limit for tungsten in FCC nickel, the HR-TEM images reveal only a substantial number of equiaxed nanocrystals, with no indication of other phases. This phenomenon occurs because, when the size of the nanocrystals is sufficiently small, the solid solution limit for atoms in the alloy correspondingly increases and the formation of probably metastable solid solutions [3,14,21,28]. The distribution of NiW (12.3 at% W) alloy nanocrystal grain size statistics is depicted in Fig. 4 (b), which average grain size is 5.7 nm.

When the tungsten content in NiW coating exceeds the threshold, a transition from nanocrystalline to amorphous structure will occur, which can be attributed to the lattice expansion due to the relatively large size of the W atoms [29]. TEM images of Ni-15.0 at% W (348K-30 A dm^{-2}) and 20.9 at% W (348K-35 A dm^{-2}) were shown in Fig. 5. For Ni-15.0 at% W alloy, no grains or boundaries were observed. A limited number of processing marks may result from the scraping action of platinum ions in FIB sampling technology. The electron diffraction pattern displays amorphous diffraction spot which suggest that single-phase amorphous was obtained by 15.0 at% W appending. TEM image and FFT spectra in rectangular frame of Ni-20.9 at% W is shown in Fig. 5 (b). The entire sample appeared amorphous, with the minor presence of black particles possibly resulting from a slight W precipitation exceeding the solution limit. However, FFT of this area displayed a single-phase amorphous diffraction spot, and XRD analysis did not reveal any crystal diffraction peaks characteristic of pure W, indicating the formation of metastable solid solutions within the system [30]. These results suggest that the synthesized nanocrystal or amorphous NiW is of high purity.

Fig. 6 displays the relationship of NiW electrodeposition alloys grain size and tungsten content and result of nonlinear fitted. The grain size of pure Ni electrodeposition coating is about 22.0 nm from previous work [31]. After a spot amount of tungsten is introduced into nickel-based coatings, the grain size significantly decreases to half of its original size which is 12.1 nm of NiW with 0.5 at% W (348K-10 A dm^{-2}). As the increase of tungsten content, under the solid solution of tungsten and segregating to the grain boundaries then negating higher energy, grain size of Ni can be further reduced through suppress grain boundary diffusion by decreasing grain boundary diffusivity [9,29]. Additionally, as the introduced of tungsten amount gradually increases, the grain size continues to decrease gradually slowing down in an approximately linear relationship. The slope of the linear relationship through the pseudo-contract is −1.35. This absolute value is close to −1.21 from literature [6]. This suggests that the current work presents a relatively small initial grain size, with numerous ultrafine grain samples

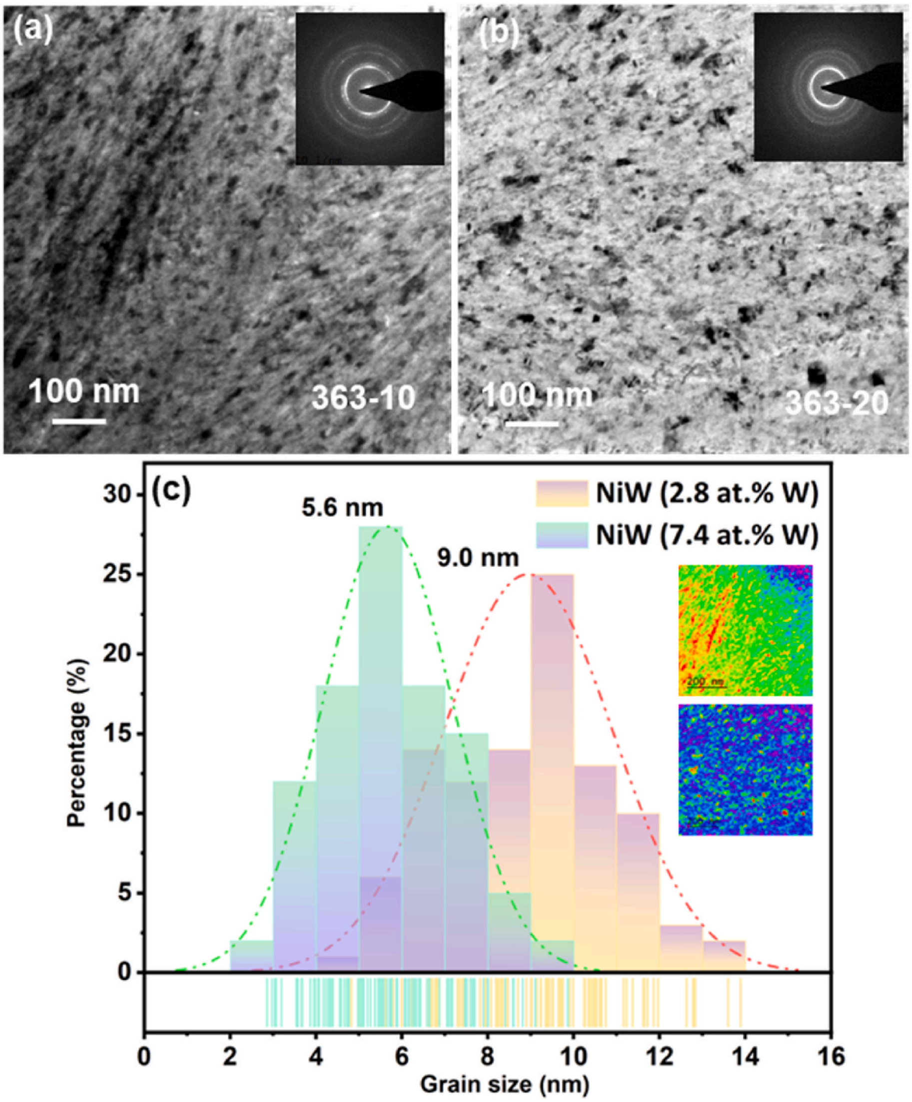

Fig. 3. TEM characterization of nanocrystal NiW. TEM images and electron diffraction patterns of nanocrystal NiW alloys with 2.8 at% W (363K-10 A dm^{-2}) (a) and 7.4 at% W (363K-20 A dm^{-2}) (b). Grain size distribution statistics images of nanocrystal NiW alloys (c).

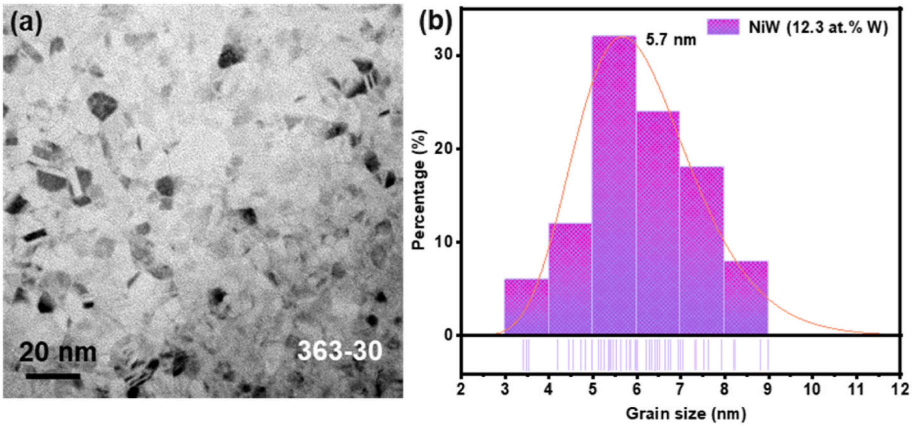

Fig. 4. TEM characterization of Ni-12.3 at%W. TEM images and electron diffraction patterns of nanocrystal NiW alloys with 12.3 at%. W (363K-30 A dm^{-2}) (a) and grain size distribution statistics images of nanocrystal NiW coating (b).

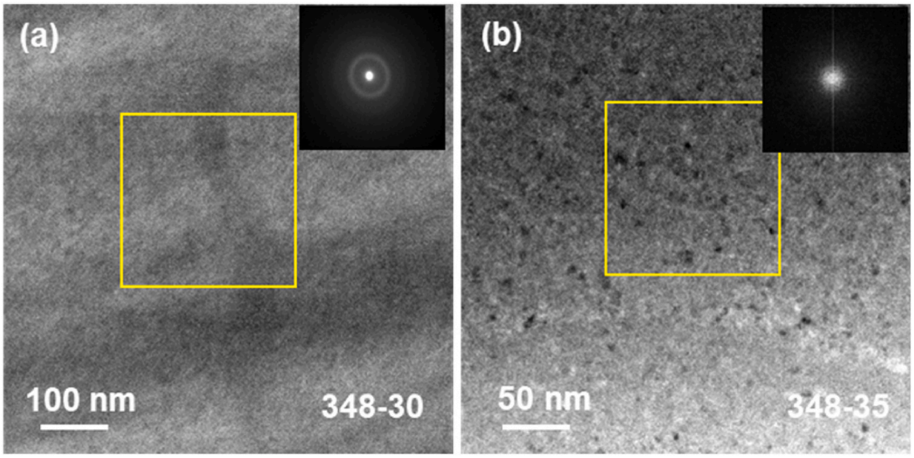

Fig. 5. TEM characterization of amorphous NiW. TEM images and electron diffraction patterns of amorphous NiW alloys with 15.0 at% W (348K-30 A dm^{-2}) (a) and 20.9 at% W (348K-35 A dm^{-2}) (b).

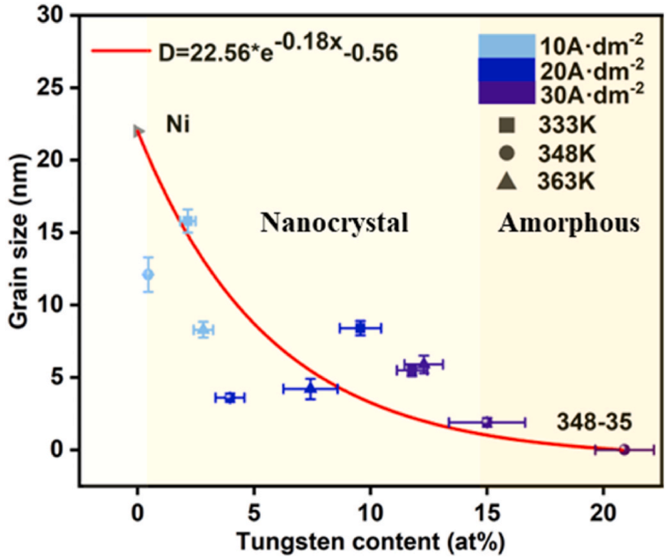

Fig. 6. Grain size and tungsten content. Relationship curve of grain size and tungsten atomic content of NiW alloy and non-linear curve fitting.

measuring less than 10 nm. Such samples are likely to reveal inverse Hall-Petch relationships, offering valuable insights for size refinement and precise material positioning of critical point. Furthermore, similar trends can be observed in other nickel-based ternary alloys like Ni-W-Fe [32]. For the Ni-9.6 at% W prepared at 333K-20 A dm^{-2}, its grain size is slightly higher than fitting curve. This relates to lower electrodeposited efficiency at moderate system temperature provides limited nucleation rate [33]. This phenomenon is consistent with the result in Fig. 2 (d). When the tungsten content reaches a sufficiently high level, the grain size decreases to below 2.0 nm obtained from 348K to 30 A dm^{-2}, transitioning NiW from nanocrystalline to an amorphous state. That is, when the tungsten content reaches 15.0 at% (348K-30 A dm^{-2}), the average grain size calculated is 1.9 nm, besides, when the W-rich NiW which tungsten content reaches 20.9 at% (348K-35 A dm^{-2}), the completely amorphous cannot calculated grain size anymore.

3.3. Microhardness and improvement

For relationship of hardness and tungsten atomic content is shown in Fig. 7. As the increase of tungsten content in NiW coatings, rising tendency dominates the curve for the surface microhardness. Overall growth trend exhibits a linear trend with a slope of 0.18 GPa/at%. The initial rapid increase can be attributed to the incorporation and solid solution of tungsten atoms in Ni. With further increases in tungsten content, the grain size decreased resulting in more grain boundaries forming, additionally more solid solution forms, impeding dislocation movement and resulting in a continued rise in strength [34,35].

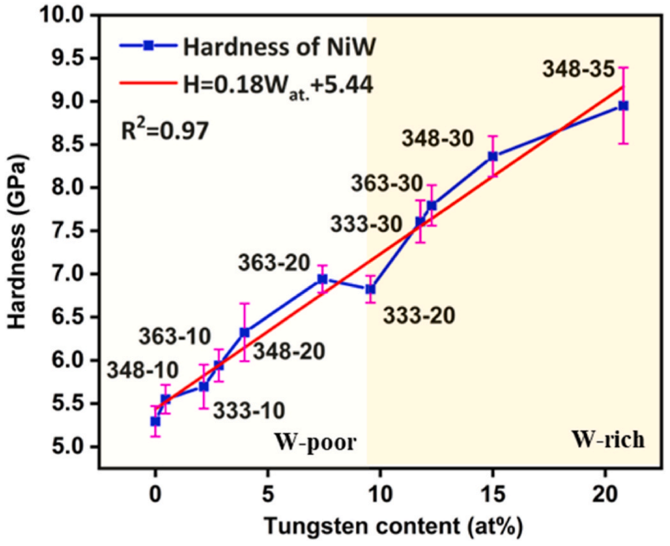

Fig. 7. Hardness and tungsten content. Curve of relationship between hardness and tungsten content of NiW alloys prepared at temperature (K)-current density (A·dm^{-2}) and fitting by linear model.

For the pure nickel at beginning of the curve, the surface hardness is a minimum value of 5.29 GPa. Afterwards, with the solid solution of tungsten in FCC nickel, the alloy immediately hardens, the hardness value of NiW with 0.5 at% W (348K-10 A dm^{-2}) reach 5.54 GPa. Since then, this upward trend has been maintained. When the tungsten content reaches the solid solution limit, the hardness of NiW has increased to around 7–8 GPa. As the tungsten content continues to increase, NiW electrodeposited alloys changes from nickel rich to tungsten rich obtained at 333K-20 A dm^{-2}, and the microstructure begins to transform from nanocrystal to amorphous. The hardness of the two amorphous coupons reaches the maximum value of the entire relationship line, which is 8.36 GPa for 15.0 at% W (348K-30 A dm^{-2}) and 8.95 GPa for 20.9 at% W (348K-35 A dm^{-2}), respectively. While there are few studies focused on the relationship between hardness and a wide range of tungsten content in NiW coatings until this consummate work, the results of present work align with trends reported in the literature [5,20, 36–39]. The process parameters, tungsten atomic content, grain size, and strength of NiW electrodeposited coatings which tungsten content were from 0.5 at% to 20.9 at% and grain size of crystal from 15.8 nm to amorphous are presented in Table 2.

3.4. Hall-Petch and inverse relationship

There have been study summarized the Hall-Petch relationship, emphasizing the interplay between dislocations, grain size, and grain boundaries [40]. It can be simplified using Eq. (1).

$$\sigma = \sigma_0 + kd^{-1/2} \tag{1}$$

The correlation between hardness and the reciprocal square root (1/sqrt) of grain size of NiW from 0 at% to 20.8 at% tungsten content is depicted in Fig. 8. For Ni and NiW electrodeposited coatings, in the Ni-rich region, Pure nickel coating has the lowest hardness value of 5.29 GPa and immediately strengthening with solid solution under tungsten atomic. As the grain size refining and decreasing (1/sqrt value increase), the hardness continues to rise until the grain size diminishes to 5.9 nm. At this point, the strength reaches its peak at 7.79 GPa. The slope *k* of the previously observed linear growth trend was 4.74. The breakdown of the Hall-Petch relation has been observed, indicating a critical point that aligns with findings presented in several studies [6]. Subsequently, as the grain size further reduces to 3.6 nm, the hardness of NiW coating experiences a slight decrease to 6.32 GPa. Notably, a transition occurs in NiW alloy's phase composition from nanocrystalline to amorphous, leading to a subsequent increase in strength. The strength values of double amorphous NiW alloy with 15.0 at% (348K-30 A dm^{-2}) and 20.9 at% (348K-35 A dm^{-2}) W measured are 8.36 GPa and 8.95 GPa, respectively, indicating that the phase transformation represents the second critical point in the transformation of strength.

For further determine the Hall-Petch relationship trend, the grain size was varied while keeping composition constant by annealing. For the Ni-15.0 at% W, the relationship cure between hardness and grain size of annealed coupons was displayed in Fig. 8 correspondingly. The grain size was calculated based on the XRD characterization results described in Fig. 2 earlier. After annealing at 673K for 2 h, the grain size of NiW with 15.0 at% W electrodeposited coating increased to 5.0 nm, resulting in a significant rise in hardness, which reached 12.62 GPa. This phenomenon can be attributed to the reverse movement of grain size within the breakdown of the Hall-Petch relationship, leading to enhanced material properties. Furthermore, additional factors such as grain boundary relaxation and solid solution atom segregation at the grain boundaries may contribute to the observed material hardening [3, 41]. As the annealed temperature continues to rise surpassing 873K for 2 h, the further increase in grain size of NiW coating results in subsequent softening. The coupon annealed at 1073K for 2 h had a maximum grain size of 25.5 nm and a hardness softening of 7.08 GPa. The overall relationship between grain size and hardness changes in NiW electrodeposition coatings with the same composition (15.0 at%) after annealed is consistent with the Hall-Petch phenomenon and its breakdown, as observed in the NiW alloys as deposited.

Table 2
Process parameter, tungsten content, grain size and hardness of nanocrystal or amorphous NiW electrodeposited alloys.

Temperature-Current density (K-A·dm^{-2})	Tungsten content (at%)	GS by XRD (nm)	GS by TEM (nm)	Hardness (GPa)
348–10	0.5	12.1		5.54
333–10	2.2	15.8		5.70
363–10	2.8	8.3	9.0	5.94
348–20	4.0	3.6		6.32
363–20	7.4	4.2	5.6	6.94
333–20	9.6	8.4		6.82
333–30	11.8	5.5		7.61
363–30	12.3	5.9	5.7	7.79
348–30	15.0	1.9	Amorphous	8.36
348–35	20.9	–	Amorphous	8.95

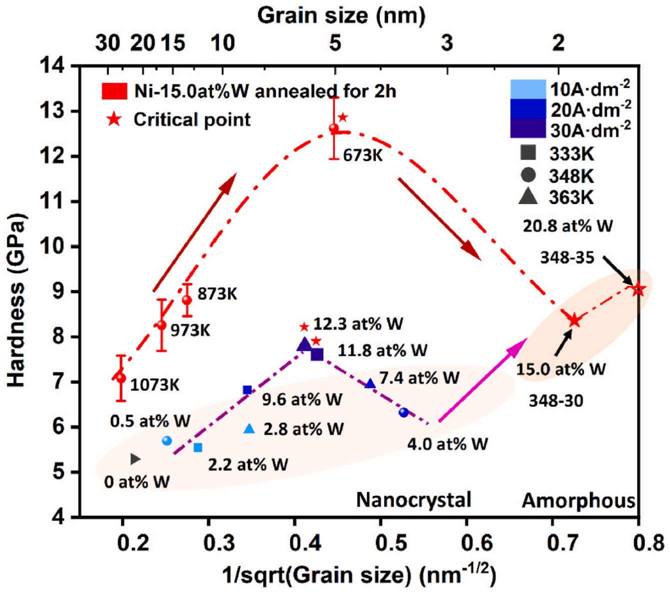

Fig. 8. Hall-Petch and inverse of NiW. Curve of relationship of hardness and sqrt of grain size and grain size of NiW and Ni-15.0 at%W annealed coatings.

4. Discussion

Grain size (GS) decreases with the various of tungsten content. It determined the hardness of NiW coatings. The GS decreases rate (η) was calculated via Eq. (2). Further, the relationship between η and tungsten atomic content was shown in Fig. 9 (a).

$$\eta = \frac{d_{Ni} - d_{Ni(W)}}{d_{Ni}} * 100\% \tag{2}$$

Where d_{Ni} is the grain size of Ni (22 nm), $d_{Ni(W)}$ represents the grain size of NiW coating as mentioned earlier. The relationship satisfies the curve fitting function. It starts to rise sharply under the tungsten atoms slightly solid solution and then slowing down to approach the peak, i.e. transferring into amorphous. More precisely, when tungsten atoms are doped into the nickel lattice, they induce significant lattice distortion and substantially increase the system's free energy. This reduction in critical nucleation work facilitates the formation of new crystal nuclei, thereby enhancing the nucleation rate and promoting grain refinement. It specifically displays as a nucleation area over the fitting curve. In contrast, systems operating at high temperatures and overvoltage experience a leveling off in the nucleation rate, which aligns with the growth rate. At this plateau, η stabilizes. Moreover, high-energy electrodeposited system further enhances the crystal growth rate, leading to a region with marginally larger grain sizes i.e., a lower η. This growth area is situated below the fitting curve in Fig. 9 (a).

Although the influence of grain size on strengthening is significantly greater than that of solid solution. Excessive solid solution content or proximity to the limitation may result in minor changes. To analyze the experimental results effectively, it is essential to separately assess the contributions of solid solution strengthening and grain refinement in NiW alloys containing various alloying elements. The solid solution strengthening can be quantified and represented by Eq. (3) [42–44].

$$Hss = G{\varepsilon_S}^{3/2}c^{1/2} \tag{3}$$

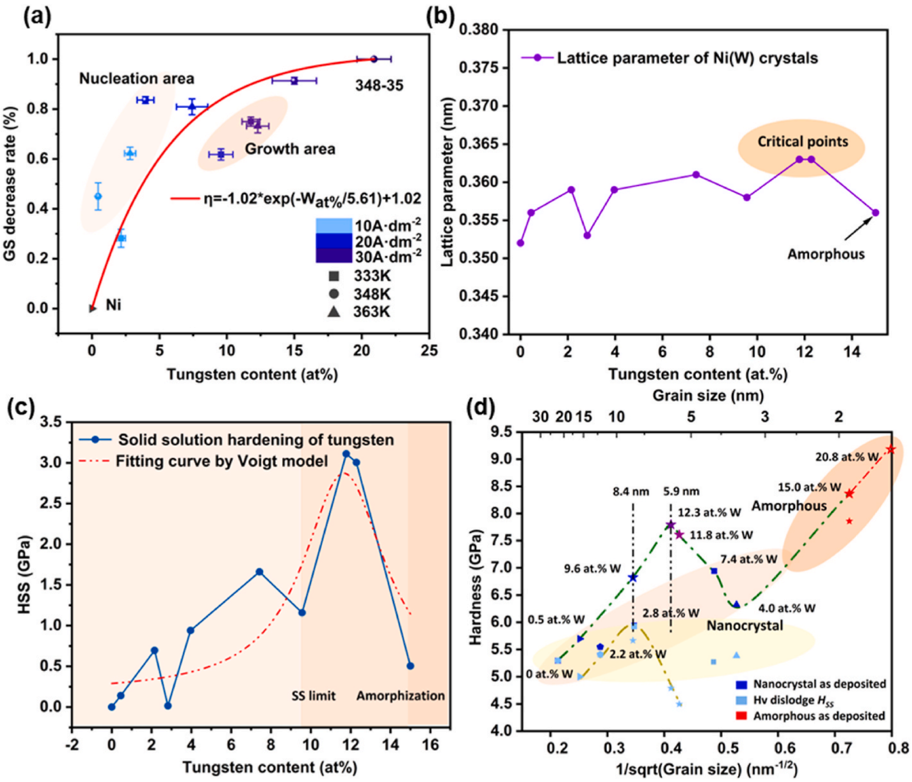

Fig. 9. *Hss* in Hall-Petch of NiW alloys. Relationship of GS decrease rate (a), lattice parameter (b), solid solution hardening (c) and tungsten atomic content of NiW coatings and the relationship of hardness (remove *Hss*) and sqrt of grain size for electrodeposited NiW coatings (d).

Where G is the shear modulus of solute, ε_s is lattice constant mismatch, c is solute atom concentration (at%). Among these parameters, G represents the shear modulus of solid solution atomic tungsten in NiW electrodeposited alloys, with a value of 161 GPa [45]. For lattice constant mismatch of FCC Ni caused by tungsten atoms, calculation was based on the previously mentioned XRD results, further details are conducted using Eqs. (4)–(6).

$$d = \frac{n\lambda}{2\sin\theta} \tag{4}$$

$$a = d \times \sqrt{h^2 + k^2 + l^2} \tag{5}$$

$$\varepsilon_S = \frac{a_{Ni(W)}}{a_{Ni}} \times 100\% \tag{6}$$

Where d is the interplanar spacing, the value of n and λ of Cu Ka is 1 and 0.154 respectively. θ is (111) peak position of FCC nickel diffraction of XRD. a is lattice parameter of Ni(W). The relationship cure between lattice parameter and tungsten content of NiW electrodeposited alloys is shown in Fig. 9 (b). The value of a_{Ni} is 0.352 nm, while the lattice parameter magnifies under the solid solution of tungsten atomics. It is noteworthy that when the tungsten content reaches 11.8 at%, the lattice parameters continue to increase, suggesting that the alloy sample has not yet exceeded the solid solution limit which consist with the result of XRD characterization. This phenomenon can be attributed to the ability of ultrafine grain sizes to accommodate a greater number of solid solution atoms [14].

The relationship between *Hss* and tungsten content in NiW electrodeposited alloys is depicted in Fig. 9 (c). Throughout the continuous solid solution process, the solid solution hardening effect progressively increases until the solid solution limit of 12.3 at% W is attained. The fitted curve exhibits a unimodal trend, suggesting that the substantial effect of solid solution strengthening at this point holds significant potential for enhancing surface hardness. The Hall-Petch relationship between hardness and grain size of NiW electrodeposited coatings in the absence of *Hss* is illustrated in Fig. 9 (d) by the corresponding light blue symbols. Similarly, as the reciprocal sqrt of grain size increases or the grain size decreases, the hardness of materials subsequently begins to rise. When the grain size diminishes to 8.4 nm, the hardness attains a maximum of 5.9 GPa then beginning to decline. Research has demonstrated that electroplated nanocrystalline Ni coatings exhibit a breakdown of the Hall-Petch relationship phenomena beyond a grain size of 12 nm, which is slightly higher than the 8.4 nm observed in present work [4]. This suggests that the solid solution strengthening of tungsten in nickel influences the Hall-Petch relationship by shifting the breakdown critical points of the material toward finer grain sizes (from 8.4 nm to 5.9 nm). Furthermore, the displacement of these characteristic points between Ni and NiW electrodeposited coatings, in the absence of *Hss*, may result from trace changes induced by other factors, such as grain boundary segregation.

The Hall-Petch plot of our results about NiW electrodeposited coatings is shown in Fig. 10, along with published results for electrodeposited pure Ni, NiCo, NiFe and NiW, plus literature and present work data for Ni-15.0 at% W where the grain size was controlled by annealing. The microhardness of coarse-grained pure Ni linearly increases as the grain size decreases. In contrast, NiCo alloys exhibits higher strength at identical grain sizes attributed to solid solution strengthening [46]. Interestingly, this effect has minimal impact on nanocrystals (less than 20 nm), indicating that the Hall-Patch relation and anomalies related to fine grain sizes overshadow the influence of solid solution [3]. While the Hall-Petch breakdown relationship in NiW alloys ranging from 20 nm to more microscopic scales and amorphous was explored.

The Hall-Petch trend is evident in our results as the larger grain sizes lie on the same line from pure Ni. After the breakdown, the strength of Ni, NiCo, NiFe and NiW alloys all have decreased as the grain size refining. Moreover, we found that it subsequently increases within the amorphous region after transformation at the terminal of curve.

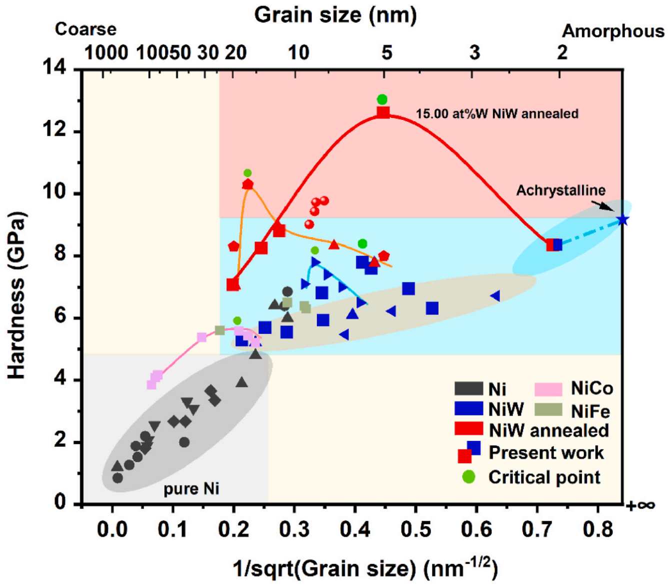

Fig. 10. Inverse Hall-Petch in Ni-based alloys. Hall-Petch plot of electrodeposited pure Ni, NiW alloys and annealed coupons (15.0 at% W), literature Ni [2,4,48], literature NiW [3,21,37], literature NiCo [46], NiFe [49] and literature annealed NiW [21,37,50].

Annealing NiW alloys containing 15.0 at% W, controlling the grain size changing at consistent element compositions, led to the discovery of a critical grain size of approximately 5.0 nm. Although grain boundary relaxation and solute atomic segregation enhancing the overall strength during heat treatment [47], the estimated inverse Hall-Petch relation characteristic points of 5.0–6.0 nm align with the findings.

Schuh et al. [3], proposed that the critical grain size of Ni-W alloys based on tungsten content can be predicted from:

$$\frac{d^i_{Ni-W}}{d^i_{Ni}} \approx \left[\frac{D_W}{D_{Ni}} \times (1-c) + c\right]^{\frac{2}{7}} \tag{7}$$

where d^i is the breakdown grain size in Ni-W alloy/pure Ni, D_W is the grain boundary diffusivity of W in Ni and D_{Ni} is the (grain boundary) self-diffusivity of Ni and c is the atomic fraction of W. The definition of the critical grain size in the annealing process of NiW alloys appears to align with the predictive model presented in Eq. (7) which has been established for predicting the critical grain size [3].

Overall, NiW alloys with varying grain sizes were fabricated spreading around critical point by adjusting temperature and current density parameters. The grain size corresponding to the Hall-Petch breakdown relationship was determined to be 5.9 nm. This result in present work addresses the limitation of limitation in materials preparation under 10 nm and failure to generate research data between 2.4 and 7.2 nm solely by adjusting a single current density factor. Furthermore, the strength transition relationship from nanocrystals to amorphous is supplemented and offered as a reference.

5. Conclusions

Nanocrystalline and amorphous NiW coatings which tungsten content controlled from 0 at% to 20.8 at% and grain size from 15.8 nm to 1.9 nm have been fabricated by electrodeposition, and their microstructure and contact-mechanical properties investigated. The main results of this work are summarized below:

1. Broad spectrum W content (from 0 at% to 20.8 at%) of nanocrystal and amorphous NiW coatings of different grain size (from 2.0 to 22.0 nm) were prepared by changing the temperature from 333K to 363K and current density from 10 A dm^{-2} to 35 A dm^{-2} of electrodeposition.
2. Grain size decreases with the elevation of tungsten content, exhibiting a trend characterized by rapid initial decrease followed by a gradual decline. When the size drops below 2 nm, it begins to transition into an amorphous phase
3. The hardness exhibits a linear increasing trend with increase in tungsten content of NiW electrodeposited coatings. The highest hardness of nanocrystal of NiW reached 7.79 GPa of 12.3 at% W and amorphous reached 8.95 GPa of 20.8 at%.
4. The Hall-Petch breakdown critical point of NiW and annealed alloys is observed below grain sizes of 5.0–6.0 nm. The solid solution hardening of NiW alloys with increasing amounts of tungsten atoms results in hardness increase. Upon removing *Hss*, the critical point of the Hall-Petch breakdown phenomenon shifts to 8.6 nm approaching Ni inverse point.
5. The increase in hardness during the nanocrystalline to amorphous transition was found to be the second changing trends critical point after the Hall-Petch breakdown.

CRediT authorship contribution statement

Zhifei Yu: Writing – original draft, Validation, Software, Methodology, Investigation, Formal analysis. **Shaojia Shi:** Methodology, Investigation. **Xingwen Zhang:** Investigation, Formal analysis. **Zesheng You:** Visualization, Data curation, Conceptualization. **Yonghao Zhao:** Writing – review & editing, Supervision, Funding acquisition, Conceptualization.

Declaration of competing interest

The authors declare that they have no known competing financial interests or personal relationships that could have appeared to influence the work reported in this paper.

Acknowledgements

Y.H. Zhao acknowledges financial supports from the National Key R&D Program of China (Grant No. 2021YFA1200203), National Natural Science Foundation of China (Grant No. 51971112 and 51225102) and Jiangsu Province Leading Edge Technology Basic Research Major Project (BK20222014) and the Fundamental Research Funds for the Central Universities (Grant No. 30919011405). The authors also want to acknowledge the support of the Jiangsu Key Laboratory of Advanced Micro-Nano Materials and Technology. SEM, TEM and EBSD experiments are performed at the Materials Characterization and Research Center of Nanjing University of Science and Technology.

Data availability

Data will be made available on request.

References

[1] J.S.C. Jang, C.C. Koch, The Hall-Petch relationship in nanocrystalline iron produced by ball milling, Scripta Metall. Mater. 24 (8) (1990) 1599–1604, https://doi.org/10.1016/0956-716x(90)90439-n.
[2] G.D. Hughes, S.D. Smith, C.S. Pande, H.R. Johnson, R.W. Armstrong, Hall-Petch strengthening for the microhardness of twelve nanometer grain diameter electrodeposited nickel, Scripta Metall. 20 (1) (1986) 93–97, https://doi.org/10.1016/0036-9748(86)90219-x.
[3] C.A. Schuh, T.G. Nieh, H. Iwasaki, The effect of solid solution W additions on the mechanical properties of nanocrystalline Ni, Acta Mater. 51 (2) (2003) 431–443, https://doi.org/10.1016/S1359-6454(02)00427-5.
[4] C.A. Schuh, T.G. Nieh, T. Yamasaki, Hall-Petch breakdown manifested in abrasive wear resistance of nanocrystalline nickel, Scr. Mater. 46 (10) (2002) 735–740, https://doi.org/10.1016/S1359-6462(02)00062-3.
[5] K.R. Sriraman, S.G.S. Raman, S.K. Seshadri, Synthesis and evaluation of hardness and sliding wear resistance of electrodeposited nanocrystalline Ni-W alloys, Mater.

Sci. Eng. A Struct. Mater. Prop. Microstruct. Process. 418 (1–2) (2006) 303–311, https://doi.org/10.1016/j.msea.2005.11.046.

[6] C.Y.A. Ong, D.J. Blackwood, Y. Li, The effects of W content on solid-solution strengthening and the critical Hall-Petch grain size in Ni-W alloy, Surf. Coating. Technol. 357 (2019) 23–27, https://doi.org/10.1016/j.surfcoat.2018.09.086.

[7] P.Q. Dai, W.C. Xu, Q.Y. Huang, Mechanical properties and microstructure of nanocrystalline nickel-carbon nanotube composites produced by electrodeposition, Mater. Sci. Eng. A Struct. Mater. Prop. Microstruct. Process. 483–84 (2008) 172–174, https://doi.org/10.1016/j.msea.2006.09.152.

[8] J. Sudagar, J.S. Lian, W. Sha, Electroless nickel, alloy, composite and nano coatings - a critical review, J. Alloys Compd. 571 (2013) 183–204, https://doi.org/10.1016/j.jallcom.2013.03.107.

[9] M. Hasegawa, G. Guillonneau, X. Maeder, G. Mohanty, J. Wehrs, J. Michler, L. Philippe, Electrodeposition of dilute Ni-W alloy with enhanced thermal stability: accessing nanotwinned to nanocrystalline microstructures, Mater. Today Commun. 12 (2017) 63–71, https://doi.org/10.1016/j.mtcomm.2017.06.002.

[10] H.Z. Fang, X.D. Hui, G.L. Chen, Effects of Mn addition on the magnetic property and corrosion resistance of bulk amorphous steels, J. Alloys Compd. 464 (1–2) (2008) 292–295, https://doi.org/10.1016/j.jallcom.2007.09.139.

[11] H.S. Ni, X.H. Liu, X.C. Chang, W.L. Hou, W. Liu, J.Q. Wang, High performance amorphous steel coating prepared by HVOF thermal spraying, J. Alloys Compd. 467 (1–2) (2009) 163–167, https://doi.org/10.1016/j.jallcom.2007.11.133.

[12] Y. Kimoto, A. Giga, T. Ohkubo, Y. Takigawa, K. Hono, K. Higashi, Ni-W amorphous/nanocrystalline duplex composite produced by electrodeposition, Mater. Trans. 48 (5) (2007) 996–1000, https://doi.org/10.2320/matertrans.48.996.

[13] T. Guo, P. Huang, F. Wang, Unusual high strain rate sensitivity of amorphous/crystalline NiW composites, Mater. Lett. 248 (2019) 189–192, https://doi.org/10.1016/j.matlet.2019.04.040.

[14] O. Younes, L. Zhu, Y. Rosenberg, Y. Shacham-Diamand, E. Gileadi, Electroplating of amorphous thin films of tungsten/nickel alloys, Langmuir 17 (26) (2001) 8270–8275, https://doi.org/10.1021/la010660x.

[15] P. Indyka, E. Beltowska-Lehman, L. Tarkowski, A. Bigos, E. García-Lecina, Structure characterization of nanocrystalline Ni-W alloys obtained by electrodeposition, J. Alloys Compd. 590 (2014) 75–79, https://doi.org/10.1016/j.jallcom.2013.12.085.

[16] L. Zhu, O. Younes, N. Ashkenasy, Y. Shacham-Diamand, E. Gileadi, STM/AFM studies of the evolution of morphology of electroplated Ni/W alloys, Appl. Surf. Sci. 200 (1–4) (2002) 1–14, https://doi.org/10.1016/S0169-4332(02)00894-2.

[17] A. Królikowski, E. Plonska, A. Ostrowski, M. Donten, Z. Stojek, Effects of compositional and structural features on corrosion behavior of nickel-tungsten alloys, J. Solid State Electrochem. 13 (2) (2009) 263–275, https://doi.org/10.1007/s10008-008-0712-2.

[18] U. Erb, A.M. El-Sherik, G. Palumbo, K.T. Aust, Synthesis, structure and properties of electroplated nanocrystalline materials, Nanostruct. Mater. 2 (4) (1993) 383–390, https://doi.org/10.1016/0965-9773(93)90180-j.

[19] A. Giga, Y. Kimoto, Y. Takigawa, K. Higashi, Demonstration of an inverse Hall-Petch relationship in electrodeposited nanocrystalline Ni-W alloys through tensile testing, Scr. Mater. 55 (2) (2006) 143–146, https://doi.org/10.1016/j.scriptamat.2006.03.047.

[20] Y.Y. Wu, D.Y. Chang, D.S. Kim, S.C. Kwon, Influence of boric acid on the electrodepositing process and structures of Ni-W alloy coating, Surf. Coating. Technol. 173 (2–3) (2003) 259–264, https://doi.org/10.1016/S0257-8972(03)00449-3.

[21] T. Yamasaki, R. Tomohira, Y. Ogino, P. Schlossmacher, K. Ehrlich, Formation of ductile amorphous & nanocrystalline Ni-W alloys by electrodeposition, Plat. Surf. Finish. 87 (5) (2000) 148–152.

[22] Gesellschaft der Wissenschaften zu Göttingen, Mathematisch-Physikalische Klasse. Fachgruppe II., Nachrichten aus der Physik, Astronomie, Geophysik, Technik, Vandenhoeck & Ruprecht, Göttingen, 1934 p 3 volumes.

[23] M. Uysal, H. Algul, E. Duru, Y. Kahraman, A. Alp, H. Akbulut, Tribological properties of Ni-W-TiO2-GO composites produced by ultrasonically-assisted pulse electro co-deposition, Surf. Coating. Technol. 410 (2021), https://doi.org/10.1016/j.surfcoat.2021.126942.

[24] M.H. Allahyarzadeh, M. Aliofkhazraei, A.R. Rezvanian, V. Torabinejad, A.R. S. Rouhaghdam, Ni-W electrodeposited coatings: characterization, properties and applications, Surf. Coating. Technol. 307 (2016) 978–1010, https://doi.org/10.1016/j.surfcoat.2016.09.052.

[25] P. Bera, M.D. Kumar, C. Anandan, C. Shivakumara, CHARACTERIZATION AND MICROHARDNESS OF ELECTRODEPOSITED Ni-W COATINGS OBTAINED FROM GLUCONATE BATH, Surf. Rev. Lett. 22 (1) (2015), https://doi.org/10.1142/S0218625x15500110.

[26] S. He, O.I. Gorbatov, P. Peng, First-principles-based statistical thermodynamic study of atomic interactions and phase stability in Ni-rich Ni-W alloys, Calphad Comput. Coupling Phase Diagrams Thermochem. 82 (2023), https://doi.org/10.1016/j.calphad.2023.102591.

[27] Z.Y. Zhang, H. Wen, J.F. Liu, P. Wang, Ni-W solid solution alloy as a high-performance catalyst for hydrazine electrooxidation, Electrochim. Acta 471 (2023), https://doi.org/10.1016/j.electacta.2023.143356.

[28] H.R. Peng, Z.Y. Jian, C.X. Liu, L.K. Huang, Y.M. Ren, F. Liu, Uncovering the softening mechanism and exploring the strengthening strategies in extremely fine nanograined metals: a molecular dynamics study, J. Mater. Sci. Technol. 109 (2022) 186–196, https://doi.org/10.1016/j.jmst.2021.08.078.

[29] A.J. Detor, C.A. Schuh, Tailoring and patterning the grain size of nanocrystalline alloys, Acta Mater. 55 (1) (2007) 371–379, https://doi.org/10.1016/j.actamat.2006.08.032.

[30] T. Yamasaki, R. Tomohira, Y. Ogino, Formation of ductile amorphous Ni-W and Fe-W electrodeposits and their nanocrystallization, Japan Inst. Meta. Proc. 12 (Jimic-3) (1999) 1247–1250. *Pts 1 and 2*.

[31] Z. Liu, Q. Zhang, X. Zhang, Z. Yu, X. Zhang, Q. Mao, J. Nie, Y. Zhao, Electrodeposition of nanocrystalline Ni and NiCr alloy coatings: effects of Cr content on microhardness and wear resistance improvement, J. Mater. Res. Technol. 30 (2024) 3584–3593, https://doi.org/10.1016/j.jmrt.2024.04.100.

[32] K.R. Sriraman, S.G.S. Raman, S.K. Seshadri, Corrosion behaviour of electrodeposited nanocrystalline Ni-W and Ni-Fe-W alloys, Mater. Sci. Eng. A Struct. Mater. Prop. Microstruct. Process. 460 (2007) 39–45, https://doi.org/10.1016/j.msea.2007.02.055.

[33] N. Eliaz, T.M. Sridhar, E. Gileadi, Synthesis and characterization of nickel tungsten alloys by electrodeposition, Electrochim. Acta 50 (14) (2005) 2893–2904, https://doi.org/10.1016/j.electacta.2004.11.038.

[34] X. Zhang, A. Misra, Superior thermal stability of coherent twin boundaries in nanotwinned metals, Scr. Mater. 66 (11) (2012) 860–865, https://doi.org/10.1016/j.scriptamat.2012.01.026.

[35] C.A. Schuh, K. Lu, Stability of nanocrystalline metals: the role of grain-boundary chemistry and structure, MRS Bull. 46 (3) (2021) 225–235, https://doi.org/10.1557/s43577-021-00055-x.

[36] Y.H. Hu, Y.D. Yu, H.L. Ge, G.Y. Wei, L. Jiang, Study on mechanical and anticorrosion performance of NiW alloy coatings prepared by induced codeposition, Int. J. Electrochem. Sci. 14 (2) (2019) 1649–1657, https://doi.org/10.20964/2019.02.19.

[37] P.C. Huang, C.C. Chou, L.S. Hsu, Preparation and tribological research of the electrodeposited Ni-W alloy coatings for piston ring application, Surf. Coating. Technol. 411 (2021), https://doi.org/10.1016/j.surfcoat.2021.126980.

[38] M.V.N. Vamsi, N.P. Wasekar, G. Sundararajan, Influence of heat treatment on microstructure and mechanical properties of pulse electrodeposited Ni-W alloy coatings, Surf. Coating. Technol. 319 (2017) 403–414, https://doi.org/10.1016/j.surfcoat.2017.03.074.

[39] E. Slavcheva, W. Mokwa, U. Schnakenberg, Electrodeposition and properties of NiW films for MEMS application, Electrochim. Acta 50 (28) (2005) 5573–5580, https://doi.org/10.1016/j.electacta.2005.03.059.

[40] E.N. Hahn, M.A. Meyers, Grain-size dependent mechanical behavior of nanocrystalline metals, Mater. Sci. Eng., A 646 (2015) 101–134, https://doi.org/10.1016/j.msea.2015.07.075.

[41] J. Hu, Y.N. Shi, X. Sauvage, G. Sha, K. Lu, Grain boundary stability governs hardening and softening in extremely fine nanograined metals, Science 355 (6331) (2017) 1292–1296, https://doi.org/10.1126/science.aal5166.

[42] Y. Wu, Y. Li, J. Lu, S. Tan, F. Jiang, J. Sun, Correlations between microstructures and properties of Cu-Ni-Si-Cr alloy, Mater. Sci. Eng., A 731 (2018) 403–412, https://doi.org/10.1016/j.msea.2018.06.075.

[43] W.F. Hosford, Mechanical Behavior of Materials, Cambridge University Press, Cambridge ; New York, 2005, p. 425, xx.

[44] Q. Mao, Y. Liu, Y. Zhao, A review on copper alloys with high strength and high electrical conductivity, J. Alloys Compd. 990 (2024) 174456, https://doi.org/10.1016/j.jallcom.2024.174456.

[45] D. Liu, Y. He, P. Hu, Z. Gan, H. Ding, A modified torsion pendulum for measuring the shear modulus of a single micro-sized filament, Acta Mech. Solida Sin. 27 (3) (2014) 221–233, https://doi.org/10.1016/S0894-9166(14)60032-X.

[46] J.A.T. Kong, M.J.R. Hache, J. Tam, J.L. McCrea, J. Howe, U. Erb, On the extrinsic Hall-Petch to inverse Hall-Petch transition in nanocrystalline Ni-Co electrodeposits, Scr. Mater. 218 (2022), https://doi.org/10.1016/j.scriptamat.2022.114799.

[47] J. Hu, Y.N. Shi, X. Sauvage, G. Sha, K. Lu, METALLURGY grain boundary stability governs hardening and softening in extremely fine nanograined metals, Science 355 (6331) (2017) 1292, https://doi.org/10.1126/science.aal5166.

[48] F. Ebrahimi, G.R. Bourne, M.S. Kelly, T.E. Matthews, Mechanical properties of nanocrystalline nickel produced by electrodeposition, Nanostruct. Mater. 11 (3) (1999) 343–350, https://doi.org/10.1016/s0965-9773(99)00050-1.

[49] J.D. Giallonardo, U. Erb, K.T. Aust, G. Palumbo, The influence of grain size and texture on the Young's modulus of nanocrystalline nickel and nickel-iron alloys, Philos. Mag. 91 (36) (2011) 4594–4605, https://doi.org/10.1080/14786435.2011.615350.

[50] C.J. Marvel, D. Yin, P.R. Cantwell, M.P. Harmer, The influence of oxygen contamination on the thermal stability and hardness of nanocrystalline Ni-W alloys, Mater. Sci. Eng. A Struct. Mater. Prop. Microstruct. Process. 664 (2016) 49–57, https://doi.org/10.1016/j.msea.2016.03.129.